Femtosecond X-ray diffraction measurements of liquids using the High Energy Density Instrument at the European X-ray Free Electron Laser

M.G. Gorman,[1] D. McGonegle,[2] R.F. Smith,[1] S. Singh,[1] T. Jenkins,[3] R. S. McWilliams,[3] B. Albertazzi,[4] S.J. Ali,[1] L. Antonelli,[5] M.R. Armstrong,[1] C. Baehtz,[6] O.B. Ball,[3] S. Banerjee,[7] A.B. Belonoshko,[8] A. Benuzzi-Mounaix,[4] C.A. Bolme,[9] V. Bouffetier,[10] R. Briggs,[1] K. Buakor,[10] T. Butcher,[7] S. Di Dio Cafiso,[6] V. Cerantola,[11] J. Chantel,[12] A. Di Cicco,[13] S. Clarke,[1] A.L. Coleman,[1] J. Collier,[7] G. W. Collins,[14] A.J. Comley,[2] F. Coppari,[1] T.E. Cowan,[6] G. Cristoforetti,[15] H. Cynn,[1] A. Descamps,[16] F. Dorchies,[17] M.J. Duff,[3] A. Dwivedi,[10] C. Edwards,[7] J.H. Eggert,[1] D. Errandonea,[18] G. Fiquet,[19] E. Galtier,[20] A. Laso Garcia,[6] H. Ginestet,[12] L. Gizzi,[21] A. Gleason,[20] S. Goede,[10] J.M. Gonzalez,[22] M. Harmand,[19,23] N. J. Hartley,[20] P.G. Heighway,[24] C. Hernandez-Gomez,[7] A. Higginbotham,[5] H. Höppner,[6] R.J. Husband,[25] T.M. Hutchinson,[1] H. Hwang,[25] A.E. Jenei,[1] D.A. Keen,[26] J. Kim,[27] P. Koester,[15] Z. Konopkova,[10] D. Kraus,[28] A. Krygier,[1] L. Labate,[15] Y. Lee,[29] H-P. Liermann,[25] P. Mason,[7] M. Masruri,[6] B. Massani,[3] E.E. McBride,[16] C. McGuire,[1] J.D. McHardy,[3] S. Merkel,[12] G. Morard,[30] B. Nagler,[20] M. Nakatsutsumi,[10] K. Nguyen-Cong,[22] A-M. Norton,[5] I.I. Oleynik,[22] C. Otzen,[31] N. Ozaki,[32] S. Pandolfi,[19] D.J. Peake,[24] A. Pelka,[6] K.A. Pereira,[33] J.P. Phillips,[7] C. Prescher,[31] T. R. Preston,[10] L. Randolph,[10] D. Ranjan,[6] A. Ravasio,[4] R. Redmer,[28] J. Rips,[28] D. Santamaria-Perez,[18] D.J. Savage,[9] M. Schoelmerich,[34] J-P. Schwinkendorf,[6] J. Smith,[7] A. Sollier,[35,36] J. Spear,[7] C. Spindloe,[7] M. Stevenson,[28] C. Strohm,[25] T-A. Suer,[14] M. Tang,[25] M. Toncian,[6] T. Toncian,[6] S.J. Tracy,[37] A. Trapananti,[13] T. Tschentscher,[10] C.E. Vennari,[1] T. Vinci,[4] S.C. Vogel,[9] T.J. Volz,[1] J. Vorberger,[6] J.P.S. Walsh,[33] J.S. Wark,[24] J.T. Willman,[22] L. Wollenweber,[10] U. Zastrau,[10] E. Brambrink,[10] K. Appel,[10] and M.I. McMahon[3]

[1)] *Lawrence Livermore National Laboratory, Livermore, CA 94550, USA*

[2)] *Atomic Weapons Establishment (AWE), Materials Science and Research Division (MSRD), Aldermaston, Berkshire, RG7 4PR, UK*

[3)] *SUPA, School of Physics and Astronomy, and Centre for Science at Extreme Conditions, The University of Edinburgh, Edinburgh EH9 3FD, UK*

[4)] *Ecole Polytechnique, Palaiseau, Laboratoire pour l'utilisation des lasers intenses (LULI), CNRS UMR 7605 Route de Saclay 91128 PALAISEAU Cedex, France*

[5)] *University of York, School of Physics, Engineering and Technology, Heslington York YO10 5DD, UK*

[6)] *Helmholtz-Zentrum Dresden-Rossendorf (HZDR), Bautzner Landstraße 400, 01328 Dresden, Germany*

[7)] *Central Laser Facility (CLF), STFC Rutherford Appleton Laboratory, Harwell Campus, Didcot OX11 0QX, UK*

[8)] *Frontiers Science Center for Critical Earth Material Cycling, School of Earth Sciences and Engineering, Nanjing University, Nanjing 210023, China*

[9)] *Los Alamos National Laboratory, Los Alamos, New Mexico 87545, USA*

[10)] *European XFEL, Holzkoppel 4, 22869 Schenefeld, Germany*

[11)] *Università degli Studi di Milano Bicocca, Dipartimento di Scienze dell'Ambiente e della Terra, Piazza della Scienza 1e4 I-20126 Milano, Italy*

[12)] *Univ. Lille, CNRS, INRAE, Centrale Lille, UMR 8207 - UMET - Unité Matériaux et Transformations, F-59000 Lille, France*

[13)] *School of Science and Technology - Physics Division, Università di Camerino, 62032 Camerino, Italy*

[14)] *University of Rochester, Laboratory for Laser Energetics (LLE), 250 East River Road Rochester NY, 14623-1299, USA*

[15)] *CNR - Consiglio Nazionale delle Ricerche, Istituto Nazionale di Ottica, (CNR - INO), Largo Enrico Fermi, 6, 50125 Firenze FI, Italy*

[16)] *School of Mathematics and Physics, Queen's University Belfast, University Road, Belfast BT7 1NN, UK*

[17)] *Université de Bordeaux, CNRS, CEA, CELIA, UMR 5107, F-33400 Talence, France*

[18)] *Universidad de Valencia - UV, Departamento de Fisica Aplicada - ICMUV, C/Dr. Moliner 50 Burjassot, E-46100 Valencia, Spain, Spain*

[19)] *Sorbonne Université, Muséum National d'Histoire Naturelle, UMR CNRS 7590, Insitut de Minéralogie, de Physique, des Matériaux, et de Cosmochinie, IMPMC, Paris, 75005, France*

[20)] *SLAC National Accelerator Laboratory, 2575 Sand Hill Road, Menlo Park, CA 94025, USA*

[21)] *CNR - Consiglio Nazionale delle Ricerche, Istituto Nazionale di Ottica, (CNR - INO), Via G. Moruzzi, 1 - 56124 Pisa, Italy*

[22)] *Department of Physics, University of South Florida, Tampa, FL 33620, USA*

[23] PIMM, Arts et Metiers Institute of Technology, CNRS, Cnam, HESAM University, 151 boulevard de l'Hopital, 75013 Paris, France
[24] Department of Physics, Clarendon Laboratory, University of Oxford, Parks Road, Oxford OX1 3PU, UK
[25] Deutsches Elektronen-Synchrotron DESY, Notkestr. 85, 22607 Hamburg, Germany
[26] ISIS Facility, STFC Rutherford Appleton Laboratory, Harwell Campus, Didcot OX11 0QX, UK
[27] Hanyang University, Department of Physics, 17 Haengdang dong, Seongdong gu Seoul, 133-791 Korea, South Korea
[28] Universität Rostock, Institut für Physik, D-18051 Rostock, Germany
[29] Yonsei University, Dept. of Earth System Sciences, 50 Yonsei-ro Seodaemun-gu, Seoul, 03722, Republic of Korea, South Korea
[30] Univ. Grenoble Alpes, Univ. Savoie Mont Blanc, CNRS, IRD, Univ. Gustave Eiffel, ISTerre, 38000 Grenoble, France
[31] Institut für Geo- und Umweltnaturwissenschaften, Albert-Ludwigs-Universität Freiburg, Hermann-Herder-Straße 5, 79104 Freiburg, Germany
[32] Osaka University, Graduate School of Engineering Science, 1-3 Machikaneyama Toyonaka Osaka 560-8531, Japan
[33] University of Massachusetts Amherst, Department of Chemistry, 690 N Pleasant St Physical Sciences Building, Amherst, MA 01003-9303, USA
[34] Paul Scherrer Institut, Forschungsstrasse 111, 5232, Villigen, Switzerland
[35] CEA, DAM, DIF, 91297 Arpajon, France.
[36] Université Paris-Saclay, CEA, Laboratoire Matière en Conditions Extrêmes, 91680 Bruyères-le-Châtel, France.
[37] Carnegie Science, Earth and Planets Laboratory, 5241 Broad Branch Road, NW, Washington, DC 20015, USA

X-ray Free Electron Laser (XFEL) sources coupled to high-power laser systems offer an avenue to study the structural dynamics of materials at extreme pressures and temperatures. The recent commissioning of the DiPOLE laser on the High Energy Density (HED) instrument at the European XFEL (EuXFEL) represents the state-of-the-art in combining X-ray diffraction with laser compression, allowing for compressed materials to be probed in unprecedented detail. Here we report quantitative structural measurements of molten Sn compressed to 85(5) GPa and ∼3500 K. The capabilities of the HED instrument enable liquid density measurements with an uncertainty of ∼1 % at conditions which are extremely challenging to reach via static compression methods. We discuss best practices for conducting liquid diffraction dynamic compression experiments and the necessary intensity corrections which allow for accurate quantitative analysis. We also provide a polyimide ablation pressure vs input laser energy for the DiPOLE drive laser which will serve future users of the HED instrument.

INTRODUCTION

The ability to probe laser-compressed samples with ultrabright, femtosecond pulses of X-rays from XFEL sources has transformed our understanding of material behaviour under dynamic compression. Indeed, there have been a number of striking results reported from XFEL studies in the last decade such as the observation of incommensurate host-guest phases forming on nanosecond timescales[1,2], exotic carbon chemistry in plastics[3,4] and the direct observation of plasticity mechanisms in Ta[5]. However, in the same time span, the number of XFEL or synchrotron studies of non-crystalline or amorphous materials has been comparatively sparse[6–9]. This is despite the fact that studying amorphous materials at high pressure using laser compression and XFELs has several advantages over performing similar experiments using static compression in the diamond anvil cell (DAC). For low-Z materials, the measured signal in static compression studies may be dominated by the large Compton scattering contribution from the opposing diamonds and so a large, pressure-dependent background must be subtracted accurately to extract the liquid scattering signal. To reach pressures beyond 200 GPa, the sample size in static compression experiments is restricted by the small (40 μm) diamond culets necessary to generate such pressures meaning data with low signal-to-noise ratios are typical. Furthermore, one also must always be conscious of the potential of sample contamination from interaction with the laser-heated diamond or pressure transmitting medium[10].

In contrast, dynamic compression can reach high-pressure and high-temperature conditions with modest laser energy - For example, 40 J of laser energy in a 10 ns pulse is sufficient to compress most metals to approximately 100 GPa and several thousand kelvin. As the target package consists only of the sample of interest and a thin ablator with low atomic number, the X-ray background is usually negligible. In addition, since the experiment occurs on nanosecond timescales, chemical reactions of the sample do not have sufficient time to occur. Previous dynamic compression studies of liquids at XFEL and synchrotrons have reported quantitative measurements, but their accuracy has been hindered by several factors such as the use of mulitple detectors which are not ideal for measuring accurate scattering intensities, limited angular coverage[6,7] or the use of a broad, asymmetric X-ray probe spectrum[8,9,11].

The capabilities of the new HED instrument at the EuXFEL overcomes these difficulties to enable high-accuracy structural determination of shock-compressed liquids. Here we compressed elemental Sn to 85(5) GPa and ∼3500 K and performed structure-factor analyses which determined a liquid density of 11.56(15) g/cm^3, in excellent agreement with previous shock compression data. We determined the coordination number of the liquid Sn to be 11.8(3), indicating behaviour similar to a simple liquid of hard spheres which is in excellent agreement with quantum molecular dynamics (QMD) simulations of liquid Sn at similar conditions.

This paper is set out to aid future users of the facility as it discusses necessary detector intensity corrections for liquid diffraction analyses and laser energy-ablation pressure relations.

EXPERIMENTAL SETUP

The experiments were performed at interaction chamber 2 (IC2) at the HED instrument at the EuXFEL[12]. A schematic of the experimental setup is displayed in Figure 1 .

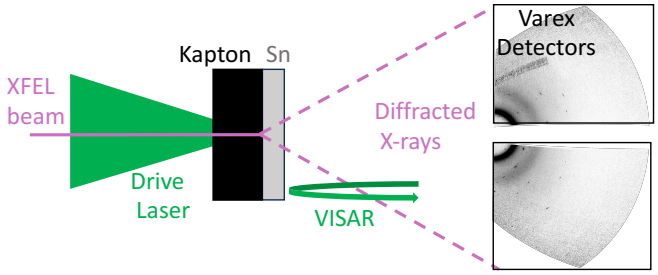

FIG. 1. **Experimental setup.** The target design consists of a 50 μm thick polyimide ablator bonded to a 20 μm thick Sn foil with a ∼1 μm glue layer. Diffraction data from laser shock compressed Sn at an estimated pressure of 85(5) GPa is shown.

The DiPOLE laser[13], which is a diode pumped ytterbium-based laser capable of up to 10 Hz operation, irradiated the sample with up to 50 J of frequency doubled (515 nm) light in a ten nanosecond pulse. The laser pulse was shaped to launch a steady ablatively driven shock into the sample and maintain a uniform pressure state for the duration of the pulse (Fig. 2). Continuous phase plates (CPPs) where used to provide a temporally stable laser spot of diameter 500 μm, 250 μm or 100 μm. The laser energy in each experiment is measured using an optic which diverts a small portion of the laser pulse to a calorimeter outside of the interaction chamber. The target package consisted of a 50 μm polyimide ablator which was bonded to a 20 μm poly-crystalline Sn foil which was purchased from Goodfellow. The targets were mounted to a Al target holder which was capable of holding up to 100 targets in a 10x10 grid with 3 mm light entrance holes spaced 11 mm apart horizontally and 10 mm vertically. The EuXFEL delivered 18.0 keV X-rays in a 50 fs pulse and the timing was adjusted such that the target was probed before the shock wave had exited the rear side. Two Varex 4343CT flat panel detectors were placed in a transmission geometry above and below the path of the XFEL beam which allowed for approximately 160° azimuthal coverage and angular coverage between 5-65 ° two theta. These detectors do not operate at the high vacuum within IC2 and so reside in an air-pocket located inside the interaction chamber. Each detector has a 400 μm Al filter which preferentially absorbs lower energy X-rays generated from the drive plasma relative to the higher-energy probe beam. A line-imaging Velocity Interferometer for Any Reflector (VISAR)[14] was used to monitor the rear surface velocity history of the samples in each experiment.

PRESSURE DETERMINATION

The IC2 uses a line imaging VISAR system to track the rear surface velocity of dynamically compressed samples. An optically transparent window is often bonded to the rear surface of the target to allow for determination of the particle velocity at the sample - window interface which is crucial for determining the peak sample pressure reached. As the shock wave breaks out at the sample-LiF interface, the interference fringes shift discontinuously with the magnitude of shift related to the particle velocity in the sample. The apparent velocity measured from the VISAR must be corrected for the refractive index of LiF which is non-linear as a function of pressure[15]. Two independent VISAR legs with different velocity sensitivities are employed to remove ambiguities in determining the correct particle velocity, and impedance matching between the sample and LiF is used to determine the sample pressure state.

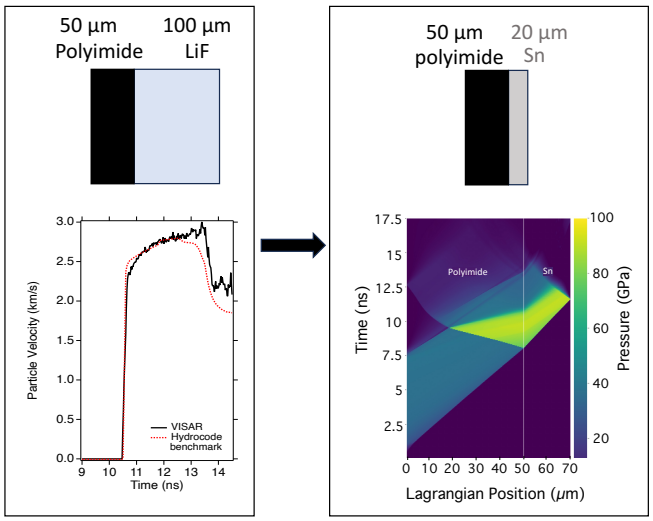

FIG. 2. **Pressure Determination** Experiments performed on polyimide - LiF targets are used to benchmark hydrodynamic simulations (left) which are then used to predict the pressure conditions reached in experiments which used polyimide-Sn targets at identical laser energies (right).

For the Sn experiments discussed here, no confining LiF window was used and therefore the particle velocity was not measured in each experiment. However, the VISAR diagnostic was able to provide accurate timing of shock break-out for

the Sn experiments which allows one to determine if the sample was probed by the X-rays when on compression or release.

To determine the conditions reached by the Sn samples we performed 1D hydrodynamic simulations[16] which were bench marked by additional experiments which used polyimide-LiF targets and identical drive energies and pulse shapes (Fig. 2). Given the stability of the DiPOLE laser (the pulse shape variance shot-to-shot was negligible) and the well constrained equations of state of polyimide and Sn at these conditions, we believe the pressure determination in Sn to be accurate to 5 %.

This calculated uncertainty in Sn pressure is related to the pressure uncertainties in the polyimide-LiF experiments which are the following: (i) the standard distribution of velocity states above the initial shock; (ii) the accuracy with which fringe shifts can be measured in the line-VISAR systems, taken here as 0.08 km/s and 0.036 km/s (5% of a fringe shift) for the two VISAR channels, respectively. Other contributors to stress uncertainty, which are considered small, relate to uncertainties in the refractive index of LiF, uncertainties in the timing of the x-ray probe with respect to the VISAR, and uncertainties in the measurements of sample thickness.

LASER ENERGY VS ABLATION PRESSURE

We performed a series of experiments on polyimide-LiF and polyimide-Cu targets at a range of laser energies with both 250 μm and 500 μm phase plates. For a known laser energy (determined by a calorimeter placed in the path of the drive beam) the peak pressure in the polyimide was determined to construct an empirical laser energy vs ablation pressure for the DiPOLE laser (Fig. 3). In the experiments using polyimide-LiF targets (plotted using black squares in Fig. 3), the peak pressure in the polyimide was determined by using the VISAR diagnostic and impedance matching from the LiF window[17,18].

In the experiments using polyimide-Cu targets (plotted using red filled and red open squares in Fig. 3), the Cu pressure was determined by fitting the diffraction pattern to a high-temperature EOS for Cu ([19,20]) and corresponding polyimide pressure was determined from impedance matching. This empirical energy vs pressure relation was found to be significantly less efficient than theoretical ablation scaling laws[21] as it was found that considerable laser energy is distributed outside of the main focal spot. This additional energy was found to potentially cause damage to adjacent targets in the holder (See Supp. Mat.). To overcome this issue, targets were positioned in every other hole on the holder to increase the distance from each other. Future improvements to the platform will include new phase plates that do not exhibit this issue. This energy vs pressure relation will allow future users to design experiments for any sample of interest and predict the conditions which can be reached using the HED instrument.

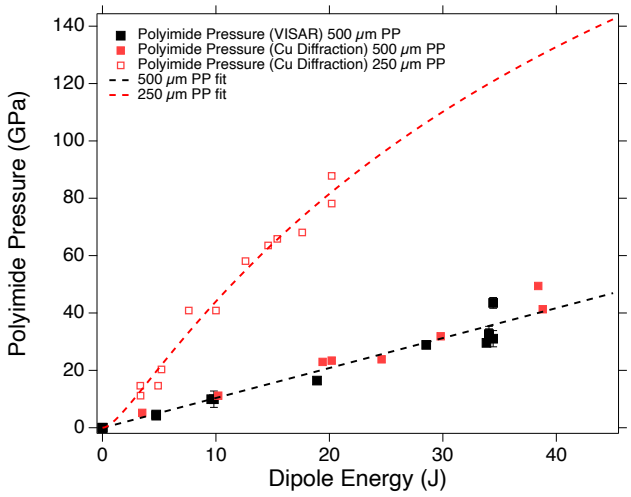

FIG. 3. **polyimide pressure as a function of laser energy for 500 μm and 250 μm phase plates.** This relation was determined by two independent methods: using impedance matching from VISAR traces from polyimide-LiF targets (black); using impedance matching from Cu diffraction data from polyimide-Cu targets (red).

X-RAY DIFFRACTION MEASUREMENTS

Experiments were performed during the #2740 experimental campaign which represented a community-wide effort and the first user experiments using DiPOLE at the HED instrument. A number of materials were investigated during this campaign but here we restrict our discussion to shock-melting of elemental Sn. The Sn samples discussed here were shock-compressed using the DiPOLE laser and the EuXFEL pulse was timed such that each sample was probed before the shock wave had travelled through the entire sample. This meant that when probed by the EuXFEL X-ray pulse, the majority of the sample existed at a uniform high-pressure, high-temperature state with a small region ahead of the shock wave at ambient conditions. This is observed in the diffraction images, with diffraction peaks from the compressed sample appearing more broad and powder-like (or diffuse in the case of liquid scattering) compared with the sharper and more textured nature of the ambient sample (Fig. 1). The diffraction peaks from the ambient signal agreed well with those predicted from the β-Sn structure (space group symmetry $I4_1/amd$, $a = 5.832$ Å, $c = 3.181$ Å) and were masked out using the X-ray analysis package Dioptas[22] to isolate the diffraction signal arising from the compressed sample. Diffraction originating from the Al target holder was also observed in some cases and was also masked out.

The detector positions and sample detector distances are precisely calibrated using a CeO_2 NIST standard with a known lattice parameter of 5.411 Å (see Supp. Mat.). For quantitative analysis of liquid samples, it is imperative to accurately measure the scattering intensity, especially at high diffraction angle. To ensure the intensity of the liquid scattering is accurate we made several corrections which included: (i) subtracting a "dark" image collected immediately before

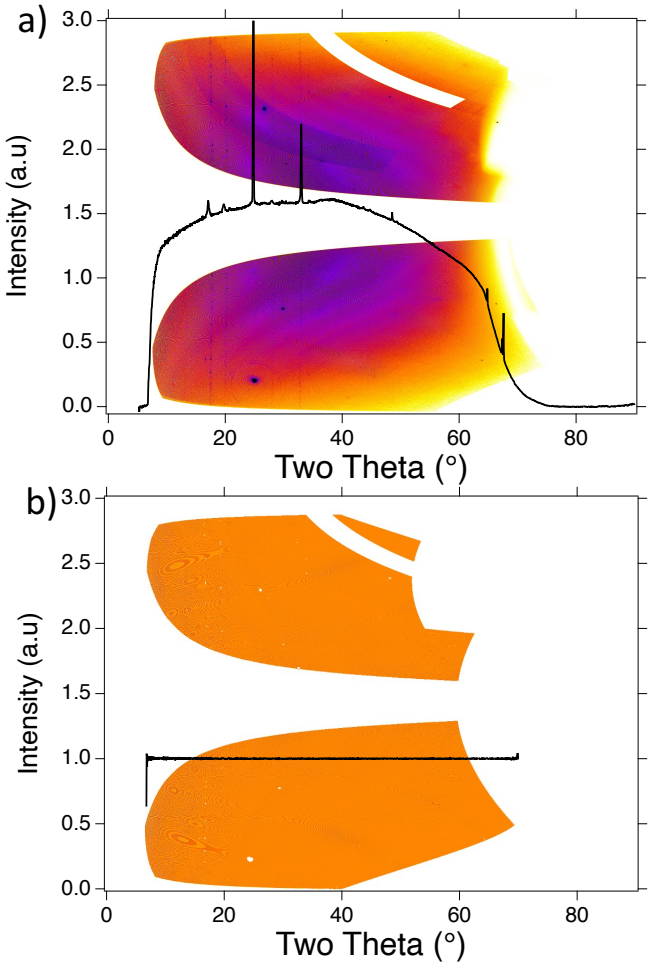

FIG. 4. **Flat-fielding the Varex detectors.** YAG crystal was illuminated with EuXFEL beam to induce fluorescence emission. (a) uncorrected image from Varex detectors with accompanying lineout. (b) Corrected image with parasitic Bragg reflections masked out.[22]

the experiment which corresponded to the average readout when no X-rays were present; (ii) the linear polarisation of the EuXFEL beam[23]; (iii) the self attenuation of the Sn sample, which becomes large at high diffraction angle (See supplementary materials); (iv) the absorption of the Al filter in front of the detectors, which is a function of diffraction angle (Fig. 4a). The Sn target design did not use a confining LiF window but for experiments in which windows are used, their contribution to the overall scattering must be considered and subtracted. This correction may become significant for target designs which use thick (500) μm windows and also samples of interest with low atomic number. The Al filter correction was achieved by irradiating a yttrium-aluminium-garnet (YAG) single crystal with the EuXFEL beam to induce a fluorescence signal. The isotropic nature of the fluorescence emission allows for the flat-fielding of each Varex detector on a pixel-by-pixel basis (Fig. 4b). These corrections were found to be crucial to enable structural analysis of the measured liquid scattering signals. The corrected intensities from each Varex detector were summed and then the combined image was azimuthally integrated to produce a 1D line out which was used for structural analysis (Fig. 5d).

Liquid structure analysis

In run 826 of the experimental campaign, a Sn sample was shock-compressed to a peak pressure of 85(5) GPa (Fig. 2) and probed by the EuXFEL beam 1 ns before shock breakout at the rear surface. The diffraction pattern shows clear evidence of liquid scattering as the diffraction maxima are broad and diffuse in nature (Fig. 5a+b).

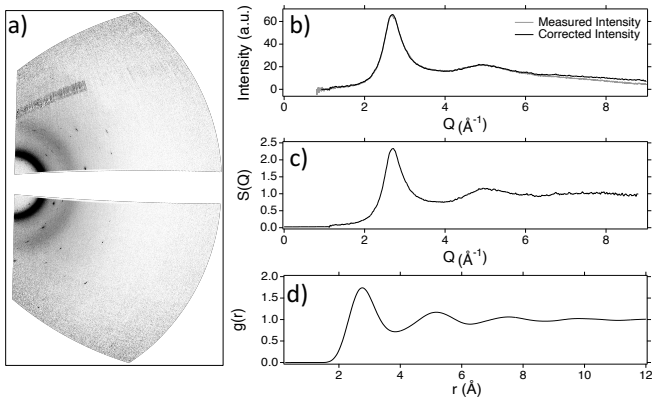

FIG. 5. **Structural analysis of liquid Sn - shot 826** (a) 2D diffraction image warped into geometric view such that diffraction rings are concentric circles. (b) 1D integrated line out from uncorrected and corrected data. (c) Optimized $S(Q)$ profile. (d) Optimized $g(r)$ profile.

The atomic structure factor is defined as

$$S(Q) = 1 + \frac{4\pi n}{Q}\int_0^\infty \left[g(r)-1\right] r sin(Qr) dr, \qquad (1)$$

where n is the average number density, r is the distance between atoms and $g(r)$ is the pair distribution function. The $S(Q)$ is obtained by scaling the diffracted intensity by the atomic scattering factor[24] and normalising it to 1 at the largest experimental Q value ($Q = \frac{4\pi\sin(\theta)}{\lambda}$ where θ is the scattering angle and λ is the X-ray wavelength). The determined structure factor is shown in Figure 5c. The $g(r)$ function (shown in Fig. 5d) is related to the probability of finding the centre of an atom at a given distance from the centre of a reference atom and is useful for monitoring structural changes in a liquid. The density of the liquid can be extracted by applying an optimisation procedure first outlined by Eggert et al.[25] which minimises a figure of merit

$$\chi^2 = \int_0^{r_{cutoff}} \left[F(r) + 4\pi n\right]^2 dr, \qquad (2)$$

where $F(r) = 4\pi n\left[g(r)-1\right]$ and r_{cutoff} represents the minimum distance at which an atom may be located from another

atom (normally equivalent to a value close to the atomic diameter). The optimisation varied three parameters: (i) a constant background signal (the initial value was taken to be 0.1); (ii) the r_{cutoff} (the initial value was selected as 1.45 Å which is the atomic diameter of Sn; (iii) and n (the initial value was set at 0.0578 which is equivalent to 11.4 g/cm^3) which is the expected density of Sn shock compressed to 85 GPa. The parameters were updated using the BOBYQA optimisation algorithm[26,27] and iterations occur until a clear minimum in χ^2 is realised.

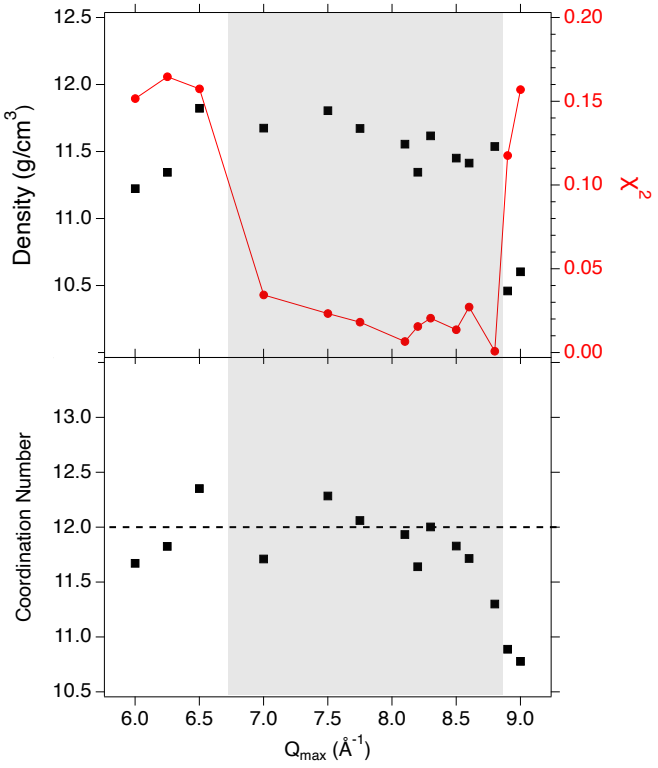

FIG. 6. **Effect of Q_{max} on optimization - shot 826.** Density and χ^2 (top) and coordination number (bottom) as determined as a function of Q_{max}. The figure of merit χ^2 (red) is minimized between 7.0-8.8 Å^{-1}.

When performing liquid structure analyses, an important value is the choice of Q_{max} which defines an upper limit of Q above which, no intensity data will be considered. As $g(r)$ is a Fourier transform of $S(Q)$ an insufficiently large Q_{max} can cause non-physical oscillations at low $g(r)$ which can inhibit the success of the liquid density optimisation described in equation 2. In contrast, a choice of Q_{max} beyond where one is confident that the intensity corrections are valid can also introduce spurious features at low $g(r)$ which can also impact the accuracy of density optimisation. The experimental geometry and choice of X-ray wavelength in these experiments allowed for data to be collected up to maximum Q values of ~9.5 Å^{-1}. The density optimisation procedure was performed for a range of Q_{max} between 6.0 Å^{-1} and 9.1 Å^{-1} (Fig. 6). As can be seen, there is a clear minimum in the χ^2 value as a function of Q_{max} between 6.8 Å^{-1} and 8.8 Å^{-1} indicating that the optimisation procedure is stable and well behaved in this range. The average density was determined to be 11.56(15) g/cm^3 which represents a 1.2 % density uncertainty from a liquid Sn sample at 85 GPa and 3500 K. The coordination number, which represents the average number of nearest neighbour atoms to a reference atom, can be expressed as

$$CN = \int_0^{r_{min}} 4\pi n r^2 g(r) dr, \tag{3}$$

where r_{min} is the location of the minimum after the first peak in $g(r)$. The coordination number of liquid Sn as a function of Q_{max} is shown in Fig. 6 and the average value within the limit of $7.0 > Q > 8.8$ was determined to be 11.9(3) indicating that liquid Sn can be described as a simple liquid at these conditions. Indeed, QMD simulations of liquid Sn at similar conditions have reported a coordination number of 12.0[8].

Shot 831 of the experimental campaign represented a repeat experiment of shot 826. A Sn target was again shock compressed to a peak pressure of 85(5) GPa and probed by the EuXFEL beam 0.5 ns before shock breakout at the rear surface. The diffraction pattern again showed clear evidence of liquid diffraction. The density was determined from the average value of individual optimisations over a Q-range where the figure of merit χ^2 is sufficiently minimised ($7 > Q > 8.8$) and was found to be 11.50(15) g/cm^3 and a coordination number of 11.9(2) (Fig. 8).

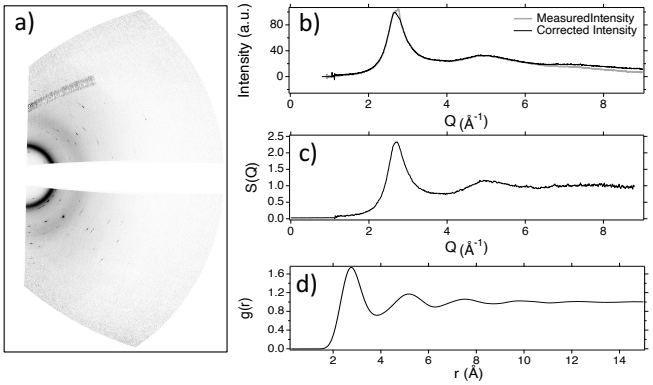

FIG. 7. **Structural analysis of liquid Sn - shot 831** (a) 2D diffraction image warped into geometric view such that diffraction rings are concentric circles. (b) 1D integrated line out from uncorrected and corrected data. (c) Optimized $S(Q)$ profile. (d) Optimized $g(r)$ profile.

DISCUSSION

Our results demonstrate that high precision structural measurements are achievable using the HED instrument at the EuXFEL at conditions which are challenging to access via static compression methods. The ability to measure liquid density at extreme pressures and temperatures is promising for many scientific fields such as planetary science. For example, understanding the density of iron-bearing silicates as a function

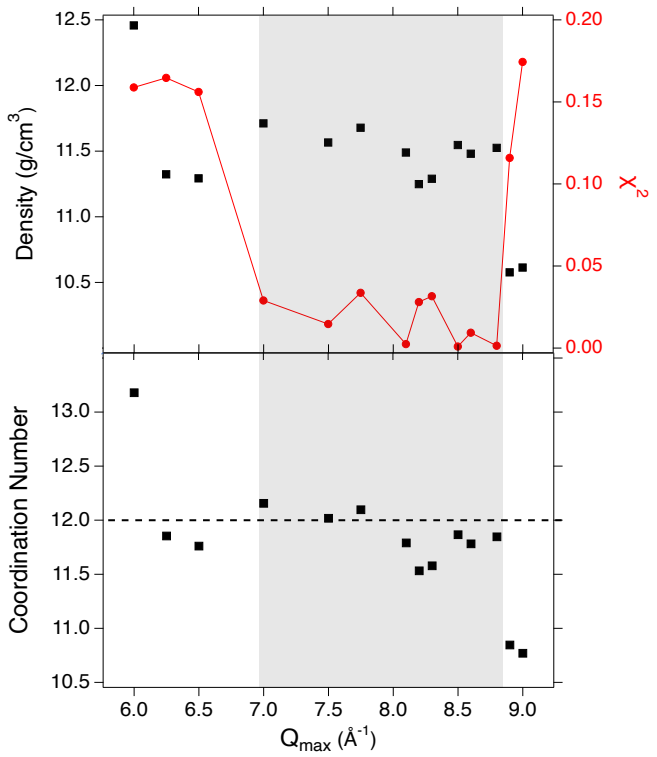

FIG. 8. **Effect of Q_{max} on optimization - shot 831.** Density and χ^2 (top) and coordination number (bottom) was determined as a function of Q_{max}. The figure of merit χ^2 (red) is minimized between 7.0-8.8 Å^{-1}.

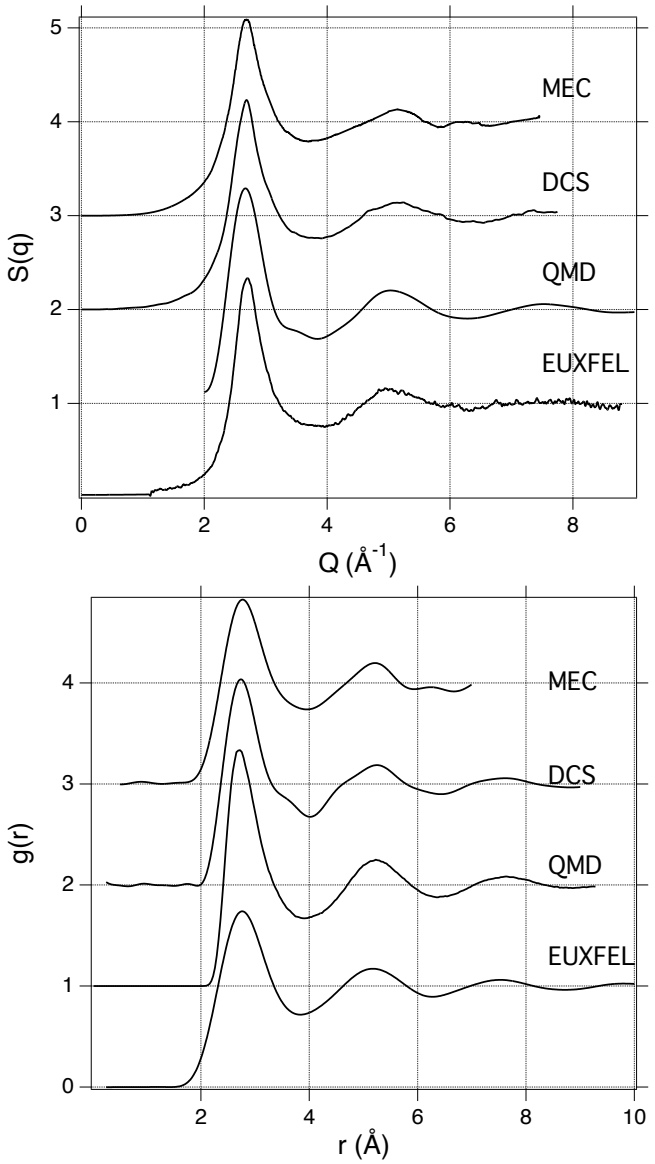

FIG. 9. **Comparison with other facilities and simulation** $S(Q)$ (a) and $g(r)$ (b) data from this work compares well with similar measurements performed at DCS and MEC as well as the results of QMD simulations performed at similar conditions. The accuracy of the measurements at MEC and DCS were hindered by experimental constraints (see text).

of pressure and the conditions of melting are key to modelling magma ocean dynamics of rocky planets[28].

The experimental setup at the HED instrument overcomes previous experimental difficulties experienced at other facilities which impacted the quality of diffraction obtained. Structure factor and pair distribution profiles of shock melted Sn from different dynamic compression facilities as well as quantum Monte Carlo simulations are shown in Figure 9. Experiments performed at MEC in 2017[7] were hindered by the limited angular coverage as well as issues surrounding the complex gain behavior of the CSPAD detectors which created artefacts in the $S(Q)$ data such as the feature at 6.2 Å^{-1} in Figure 9. Since 2017, the operating X-ray energy at MEC is now up to 25 keV and there is an effort to soon field the same Varex detectors as used in the experiments reported here. Both improvements will dramatically improve the quality of liquid diffraction data obtainable at this facility. Experiments performed at DCS in 2021[8] had sufficient angular coverage and a robust large area detector, but used a broad, asymmetric X-ray source. While a correction was applied to these data to account for source energy asymmetry, the correction impacted the accuracy with which the density could be determined and also introduced spurious features in the $g(r)$ profiles such as the features at 3.5Å and 4.5 Å in Figure 9. The APS synchrotron is currently undergoing an upgrade which will mean the X-ray source will be highly monochromatic thus improving the quality of liquid diffraction data obtainable at this facility. The data collected at the EuXFEL overcomes these experimental difficulties with the use of large-area scintillator based detectors, a high X-ray energy (18 keV) and highly monochromatic X-ray source ($\frac{\Delta E}{E} = 0.1\%$) to achieve $S(Q)$ and $g(r)$ profiles which are in excellent agreement with those produced from QMD simulations at similar conditions.

In summary we have demonstrated that high quality liquid diffraction measurements including novel density contrast measurements of a sample as it melts are possible using the HED instrument at the EuXFEL. Using shock compressed Sn as an example, we reported liquid density measurements with uncertainties of 1.2 % at a pressure of 85(5) GPa and ∼3500

K. We have discussed the intensity corrections which are necessary for the quantitative analysis of the liquid diffraction data, as well as the methods for determining the sample pressure history. We have also provided a laser energy vs polyimide ablator pressure relations which will be useful to users planning future experiments at the facility.

[1]R. Briggs, *et al.*, Ultrafast x-ray diffraction studies of the phase transitions and equation of state of scandium shock compressed to 82 GPa. *Physical review letters* **118**, 025501 (2017).

[2]A. Coleman, *et al.*, Identification of phase transitions and metastability in dynamically compressed antimony using ultrafast x-ray diffraction. *Physical review letters* **122**, 255704 (2019).

[3]D. Kraus, *et al.*, Formation of diamonds in laser-compressed hydrocarbons at planetary interior conditions. *Nature Astronomy* **1**, 606–611 (2017).

[4]Z. He, *et al.*, Diamond formation kinetics in shock-compressed C H O samples recorded by small-angle x-ray scattering and x-ray diffraction. *Science Advances* **8**, eabo0617 (2022).

[5]C. E. Wehrenberg, *et al.*, In situ x-ray diffraction measurement of shock-wave-driven twinning and lattice dynamics. *Nature* **550**, 496–499 (2017).

[6]M. Gorman, *et al.*, Femtosecond diffraction studies of solid and liquid phase changes in shock-compressed bismuth. *Scientific reports* **8**, 16927 (2018).

[7]R. Briggs, *et al.*, Coordination changes in liquid tin under shock compression determined using in situ femtosecond x-ray diffraction. *Applied Physics Letters* **115** (2019).

[8]S. Singh, *et al.*, Quantitative analysis of diffraction by liquids using a pink-spectrum x-ray source. *Journal of Synchrotron Radiation* **29**, 1033–1042 (2022).

[9]A. L. Coleman, *et al.*, Quantitative measurements of density in shock-compressed silver up to 330 gpa using x-ray diffraction. *Journal of Applied Physics* **131** (2022).

[10]S. Anzellini, S. Boccato, A practical review of the laser-heated diamond anvil cell for university laboratories and synchrotron applications. *Crystals* **10**, 459 (2020).

[11]S. Singh, *et al.*, A structural study of hcp and liquid iron under shock compression up to 275 gpa. *arXiv preprint arXiv:2304.07933* (2023).

[12]U. Zastrau, *et al.*, The high energy density scientific instrument at the european xfel. *Journal of synchrotron radiation* **28**, 1393–1416 (2021).

[13]P. Mason, *et al.*, Development of a 100 j, 10 hz laser for compression experiments at the high energy density instrument at the european xfel. *High Power Laser Science and Engineering* **6**, e65 (2018).

[14]P. M. Celliers, *et al.*, Line-imaging velocimeter for shock diagnostics at the OMEGA laser facility. *Review of Scientific Instruments* **75**, 4916–4929 (2004).

[15]L. Kirsch, *et al.*, Refractive index of lithium fluoride to 900 gigapascal and implications for dynamic equation of state measurements. *Journal of Applied Physics* **125** (2019).

[16]J. T. Larsen, S. M. Lane, Hyades—a plasma hydrodynamics code for dense plasma studies. *Journal of Quantitative Spectroscopy and Radiative Transfer* **51**, 179–186 (1994).

[17]P. Celliers, G. Collins, D. Hicks, J. Eggert, Systematic uncertainties in shock-wave impedance-match analysis and the high-pressure equation of state of al. *Journal of applied physics* **98** (2005).

[18]G. I. Kerley, Calculation of release adiabats and shock impedance matching. *arXiv preprint arXiv:1306.6913* (2013).

[19]T. S. Sokolova, P. I. Dorogokupets, A. M. Dymshits, B. S. Danilov, K. D. Litasov, Microsoft excel spreadsheets for calculation of p–v–t relations and thermodynamic properties from equations of state of mgo, diamond and nine metals as pressure markers in high-pressure and high-temperature experiments. *Computers & Geosciences* **94**, 162–169 (2016).

[20]J. D. McHardy, C. V. Storm, M. J. Duff, S. G. Macleod, M. I. McMahon, On the creation of thermal equations of state for use in dioptas. *High Pressure Research* **43**, 40–57 (2023).

[21]R. P. Drake, R. P. Drake, *Introduction to high-energy-density physics* (Springer, 2006).

[22]C. Prescher, V. B. Prakapenka, Dioptas: a program for reduction of two-dimensional x-ray diffraction data and data exploration. *High Pressure Research* **35**, 223–230 (2015).

[23]K. S. Schulze, *et al.*, Towards perfectly linearly polarized x-rays. *Physical Review Research* **4**, 013220 (2022).

[24]J. H. Hubbell, *et al.*, Atomic form factors, incoherent scattering functions, and photon scattering cross sections. *Journal of physical and chemical reference data* **4**, 471–538 (1975).

[25]J. H. Eggert, G. Weck, P. Loubeyre, M. Mezouar, Quantitative structure factor and density measurements of high-pressure fluids in diamond anvil cells by x-ray diffraction: Argon and water. *Physical Review B* **65**, 174105 (2002).

[26]M. J. Powell, *et al.*, The bobyqa algorithm for bound constrained optimization without derivatives. *Cambridge NA Report NA2009/06, University of Cambridge, Cambridge* **26** (2009).

[27]C. Cartis, J. Fiala, B. Marteau, L. Roberts, Improving the flexibility and robustness of model-based derivative-free optimization solvers. *ACM Transactions on Mathematical Software (TOMS)* **45**, 1–41 (2019).

[28]R. Caracas, K. Hirose, R. Nomura, M. D. Ballmer, Melt–crystal density crossover in a deep magma ocean. *Earth and Planetary Science Letters* **516**, 202–211 (2019).

DATA AVAILABILITY

Raw data for this publication were obtained during the 2740 community experiment at the European XFEL (runs xxx, xxx, xxx). Raw data are available at (provide doi link from XFEL) and the corresponding calibrations are provided in the supplementary materials.

ACKNOWLEDGEMENTS

We acknowledge the European XFEL in Schenefeld, Germany, for provision of X-ray free electron laser beam time at the Scientifc Instrument HED (High Energy Density Science) and would like to thank the staff for their assistance. The authors are indebted to the HIBEF user consortium for the provision of instrumentation and staff that enabled this experiment. The data is available upon reasonable request [10.22003/XFEL.EU-DATA-002740-00]

Part of this work was performed under the auspices of the U.S. Department of Energy by Lawrence Livermore National Laboratory under Contract No. DE-AC52-07NA27344 and was supported by the Laboratory Directed Research and Development Program at LLNL (project 21-ERD-032).

Part of this work was performed under the auspices of the U.S. Department of Energy through the Los Alamos National Laboratory, operated by Triad National Security, LLC, for the National Nuclear Security Administration (Contract No. 89233218CNA000001). Research presented in this Letter was supported by the Department of Energy, Laboratory Directed Research and Development program at Los Alamos National Laboratory under Project Number 20190643DR and at SLAC National Accelerator Laboratory, under contract DE-AC02-76SF00515.

This work was supported by Grants No. EP/S022155/1 (MIM, MJD) and EP/S025065/1 (JSW, DJP, PGW) from the UK Engineering and Physical Sciences Research Council.

JDM is grateful to AWE for the award of CASE Studentship P030463429

PGH acknowledges support from the Oxford Centre for High Energy Density Science (OxCHEDS) under PDRA contract 30469604.

EEM and AD were supported by the UK Research Innovation Future Leaders Fellowship (MR/W008211/1) awarded to EEM. DE and DS from Univ. de Valencia thanks the financial support by the Spanish Ministerio de Ciencia e Innovación (MICINN) and the Agencia Estatal de Investigación (MCIN/AEI/10.13039/501100011033) under grants PGC2021-125518NB-I00 and PID2022-138076NB-C41 (cofinanced by EU FEDER funds), and by the Generalitat Valenciana under grants CIPROM/2021/075, CIAICO/2021/241 and MFA/2022/007 (funded by Next Generation EU PRTR-C17.I1). NJH and AG were supported by the DOE Office of Science, Fusion Energy Science under FWP 100182.

This material is based upon work supported by the Department of Energy National Nuclear Security Administration under Award Number DE-NA0003856 (GWC, T-AS)

BM and RSM acknowledge funding from the European Research Council (ERC) under the European Union's Horizon 2020 research and innovation programme (Grant agreement No. 101002868)

KA, KB, ZK, HPL, RR and TT thank the DFG for support within the Research Unit FOR 2440.

YL is grateful for the support from the Leader Researcher program (NRF-2018R1A3B1052042) of the Korean Ministry of Science and ICT (MSIT)

SM, HG, and JC are funded by the the European Union (ERC, HotCores, Grant No 101054994). Views and opinions expressed are however those of the author(s) only and do not necessarily reflect those of the European Union or the European Research Council. Neither the European Union nor the granting authority can be held responsible for them.

COMPETING INTERESTS

The authors declare no competing interests.